Journal of Alloys and Compounds 489 (2010) 215–223

Contents lists available at ScienceDirect

Journal of Alloys and Compounds

journal homepage: www.elsevier.com/locate/jallcom

Photoluminescence in laser ablated nanostructured indium oxide thin films

D. Beena [a], K.J. Lethy [a], R. Vinodkumar [a], A.P. Detty [a], V.P. Mahadevan Pillai [a,*], V. Ganesan [b]

[a] Department of Optoelectronics, University of Kerala, Kariavattom 695581, Thiruvananthapuram, Kerala, India
[b] UGC-DAE Consortium for Scientific Research, Khandwa Road, Indore 452017, Madhya Pradesh, India

ARTICLE INFO

Article history:
Received 27 March 2009
Accepted 10 September 2009
Available online 19 September 2009

Keywords:
Pulsed laser ablation
Transparent conducting oxides
Nanocrystalline indium oxide films
Quantum confinement
Photoluminescence
Gas sensing

ABSTRACT

Nanocrystalline indium oxide films have been deposited using pulsed laser ablation technique at different substrate temperatures and the films are post-annealed at different temperatures. The structural, optical and electrical properties of the films are investigated by XRD, SEM, AFM, UV–vis spectra, photoluminescence spectra and electrical conductivity measurements. X-ray diffractograms of the as-deposited and post-annealed films A–C show that films are amorphous at lower substrate temperatures and transform to mixture of amorphous and crystalline phases. The grain size determination based on Debye Scherrer's formula shows that the average grain size of the crystallites in the films ranges from 6 to 32 nm. Dislocation density, biaxial strain, lattice strain and lattice stress of the films are also calculated. SEM micrographs show that all the films are densely packed with the crystallites in the nanodimensions. SEM images show porous nanocrystalline nature for the films of samples B and C which make them suitable for gas sensing. The as-deposited samples show decrease in resistivity with increase in substrate temperature and the lowest resistivity obtained is $6.6 \times 10^{-5}\ \Omega$ m for the as-deposited films at substrate temperature 773 K. Efficient photoluminescence emission is observed in all the films and this can be attributed to higher values of rms surface roughness exhibited by these films. In_2O_3 films exhibit a PL emission property in the UV region at room temperature which suggests possible applications in nanoscale optoelectronic devices in the future.

1. Introduction

Indium oxide (In_2O_3) is a n-type semiconductor with a direct band gap (3.5–3.7 eV) [1] and an indirect band gap ~2.6 eV [2]. Indium oxide (abbreviated as INO) has a complex cubic bixbyte structure originating from an array of unoccupied tetrahedral oxygen anion sites. The n-type semiconducting nature of INO is due to the deviations from stoichiometric composition and the excess indium atoms or oxygen vacancies can serve as donors. The material properties of INO described in the literature often differ considerably from each other, owing to different preparation conditions and different oxidation states of the samples. Low dimensional and nanostructured semi-conducting oxides, e.g. ZnO [2], CdO [3] and In_2O_3 [1,4] have recently attracted much attention due to their novel properties differing from those of thin films, and due to their applications in nanoelectronics, photonics and sensor technology. Indium oxide nanoparticles are used for transparent conductive coatings and as electrically conductive thin films in modern electronics and optoelectronics. One-dimensional In_2O_3 nanostructures have been demonstrated to be sensitive to NO_2 and NH_3 gases [5,6] as well as to biomolecules [7]. In_2O_3 thin films have been used as active layers in ozone (O_3) gas sensors [8–10]. They are also used in solar cells, transparent electrodes for hetero-junction solar cells, liquid crystal displays [11,12] and antireflection coatings for silicon solar cells [13,14]. Thermal annealing is a widely used method to improve crystal quality and to study structural defects in materials and to activate dopants and to alloy ohmic contacts in semiconductors. During the annealing process, dislocations and other structural defects will move in the material and adsorption/decomposition will occur on the surface, thus the structure and stoichiometric ratio of the material will change. The structural and optical properties are vital for semiconductor devices especially for light emitting devices [12].

Despite the impressive advancement in INO based devices, many material properties of INO are not yet well understood, such as the role of various defects in the material and their effect on device performance. There are only a few reports on photoluminescence properties of intrinsic indium oxide. Photoluminescence study of INO nanoparticles dispersed within pores of mesoporous silica annealed at different temperatures are reported by Zhou et al. [15]. Zhang et al. [16] reported PL band in the wavelength range of 300–360 nm for nanowire arrays formed on anodic alumina membranes by electrodeposition technique. A strong PL emission peak at 398 nm was detected upon excitation of In_2O_3 nanowires embedded in alumina template at 274 and 305 nm under room temperature [17]. However the photoluminescence of laser ablated INO

* Corresponding author. Tel.: +91 471 2412167.
E-mail address: vpmpillai9@gmail.com (V.P. Mahadevan Pillai).

0925-8388/$ – see front matter © 2009 Elsevier B.V. All rights reserved.
doi:10.1016/j.jallcom.2009.09.055

films on quartz substrates is not studied so far. Hence an investigation of photoluminescent properties of laser ablated INO films on quartz substrate as a function of substrate temperature and annealing temperature is of interest in the research point of view. In the present investigation indium oxide films are prepared on quartz substrates at different substrate temperatures (T_S) viz., 473, 623 and 773 K using non-reactive pulsed laser ablation technique. The as-deposited and annealed films are characterized by X-ray diffraction, scanning electron microscopy, atomic force microscopy, UV–vis spectroscopy, photoluminescence spectroscopy and DC electrical resistivity measurements.

2. Experimental details

The deposition of the films is carried out inside a multi-port stainless steel vacuum chamber equipped with a gas inlet, a rotating multi-target and a substrate holder which can be heated up to 800 °C. The irradiations are performed using a Q-switched Nd:YAG laser (Quanta–Ray INDI – Series, Spectra Physics) with frequency doubled 532 nm radiation having a pulse width 7 ns and repetition frequency 10 Hz. In_2O_3 (Merck, purity 99.995%) powder is grinded well in an agate mortar for 2 h, pressed into 11 mm diameter and 3 mm thickness pellet at 1.5 ton and then sintered at 1350 °C for 7 h in air. Sintered INO pellets are used for ablation on quartz substrates. The target is rotated with constant speed during ablation to avoid pitting of target at any given spot and to obtain uniform thin films. The laser radiation is impinged on the target at 45° with respect to the normal. Before irradiations, the deposition chamber is evacuated down to a base pressure of 4×10^{-6} mbar. The quartz substrate is fixed at an on-axis distance of 7 cm from the target and the deposition is done in non-reactive atmosphere at different substrate temperatures namely 473, 623 and 773 K (films designated as A, B and C respectively). The energy density of the laser beam at the target surface is maintained at 2 J/cm^2 during deposition and the duration of deposition is 30 min for all the films. The film A is post-annealed at temperatures viz. 473, 773 and 973 K, whereas B and C films are post-annealed at 773 and 973 K using a programmable furnace. During heating the temperature is allowed to rise at a rate of 3 °C/min. and the films are maintained at the respective temperatures for 1 h in furnace and then cooled to room temperature naturally. X-ray diffraction measurements of the films are performed using X-pert Pro Netherland Cu-Ka (1554) 40 kV, 30 mA. All X-ray diffractograms are taken with the same parameters, such as 2θ between 20° and 70° and scan speed of 2°/min. The microstructure and surface morphology of the films are studied using JEOL, jsm-5600 scanning electron microscope. Surface morphology of the films at nanometric scale was investigated by AFM (Digital Instruments Nanoscope E, Si_3N_4 100 μm cantilever, 0.58 N/m force constant) measurements in contact mode. Grain size and root mean square (rms) surface roughness of the deposited films are determined on a scan area of 2 μm × 2 μm using WSxM software of Nano Tech. Electronica. A double beam spectrophotometer (Type JASCO, V-550, UV–vis–NIR) with automatic computer data acquisition, with photometric accuracy of ±0.002–0.004 absorbance and 0.3% transmittance is employed to record the optical transmittance and reflectance spectra of the deposited films over the wavelength range of 190–900 nm at normal light incidence. A clean quartz substrate identical to the substrate used for film deposition is used as a reference to record the absolute transmission whereas $BaSO_4$ crystal is used as a reference for reflectance studies of the deposited film. The optical constants of the films like refractive index, extinction coefficient and optical band gap are evaluated from the measured transmittance and reflectance spectra. Room temperature photoluminescence spectra of the films are recorded using Horiba Jobin Yvon Flourolog III modular spectroflourometer equipped with 450 W Xenon lamp and Hamatsu R928-28 photomultiplier with a computer attached to the setup. DC electrical resistivity of the films is measured by four-probe method using Keithley 2400 source meter with 21 V and 0.1 μA.

3. Results and discussion

The thicknesses of the films are measured using interferrometric technique and are found to be in the range in the order of 120–215 nm.

3.1. X-ray diffraction results

X-ray diffractograms of the as-deposited and post-annealed films A–C are shown in Figs. 1–3. All the XRD patterns show a broad hump like feature around $2\theta = 20°$ which can be due to the amorphous nature of the substrate or the nanocrystalline nature of the films [18]. Analysis of XRD pattern suggests that, the microstructural evolution and transformation kinetics from amorphous to crystalline phase is dependent on both substrate temperature and annealing temperature. The as-deposited A film is amorphous in nature whereas as-deposited B film is quasi-crystalline and the as-deposited C film is polycrystalline in nature. Increase of substrate temperature enhances kinetic energy and hence the mobility of the surface species. This can be the reason for improved crystallinity of the films deposited at higher substrate temperature.

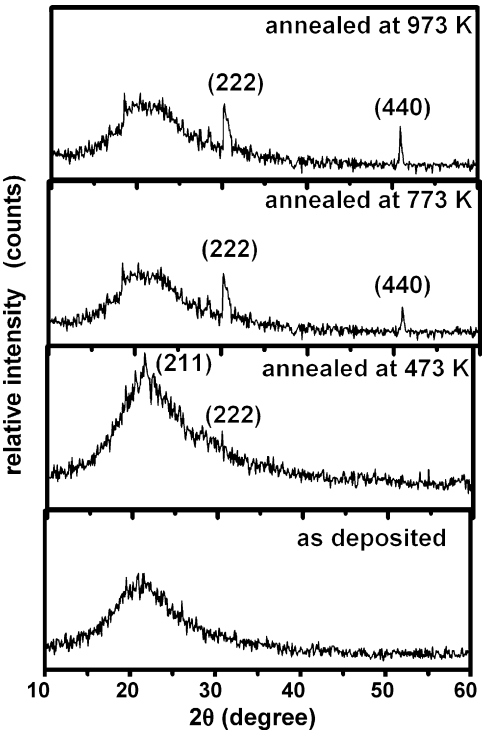

Fig. 1. GIXRD patterns of as-grown laser ablated indium oxide film deposited at T_s = 473 K and its post-annealed films at different annealing temperatures.

The post-annealed film A at annealing temperature (T_{ANN}) 473 K shows a less intense peak corresponding to (2 1 1) lattice reflection plane. The XRD patterns of A films annealed at T_{ANN} = 773 K and T_{ANN} = 973 K show peaks corresponding to (2 2 2) and (4 4 0) lattice reflection planes. The film annealed at 773 K shows a preferred orientation along (2 2 2) direction corresponding to cubic phase of indium oxide [19] whereas the film annealed at 973 K does

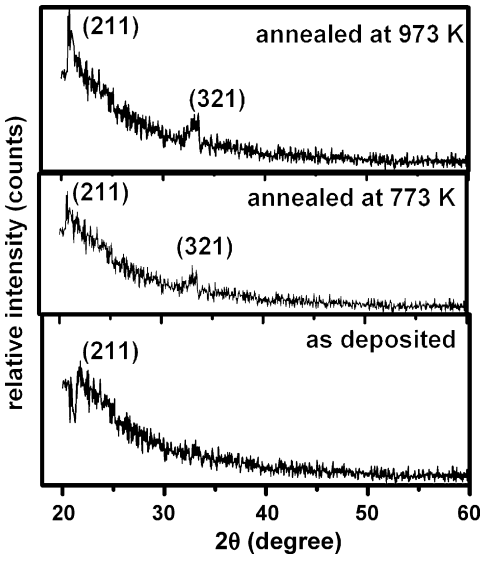

Fig. 2. GIXRD patterns of as-grown laser ablated indium oxide film deposited at T_s = 623 K and its post-annealed films at different annealing temperatures.

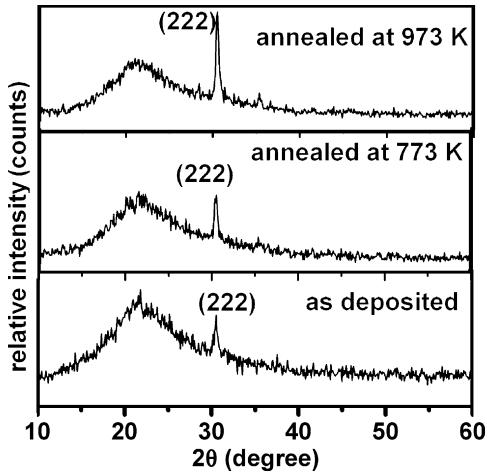

Fig. 3. GIXRD patterns of as-grown laser ablated indium oxide film deposited at T_s = 773 K and its post-annealed films at different annealing temperatures.

not show any preferred orientation. The enhanced intensity of XRD peaks at higher annealing temperatures is an indication of increase in crystallinity with increase in annealing temperature.

The XRD pattern of as-deposited B film shows a less intense peak at (2 1 1) lattice reflection plane. As the annealing temperature increases the intensity of this peak enhances. In the XRD patterns of B films annealed at 773 and 973 K, an additional peak corresponding to (3 2 1) plane is also observed. But in the XRD pattern of bulk cubic indium oxide (3 2 1) plane and (2 1 1) plane are very less intense compared to (2 2 2) and (4 4 0) planes [19]. Interestingly the prominent peaks of cubic indium oxide planes corresponding to (2 2 2) and (4 4 0) are not found in these films. Many of the reports show that the intensity and orientation of the XRD peaks corresponding to nanostructured films can vary widely from that of the bulk material. This is because the preferred orientation of crystalline growth is strongly depending on the deposition conditions of the films.

The XRD patterns of as-deposited C film and its post-annealed counter parts at different annealing temperatures present a single crystalline like structure (cubic phase) with preferred orientation along (2 2 2) plane. The films are less crystalline even at high substrate temperatures due to defects and lack of enough kinetic energy and mobility of the grains to get oriented at respective planes. Defects/imperfections/oxygen vacancies of the crystal lattice decrease on post-annealing. Annealing enhances thermal energy and the average size of the crystallites (D) of In_2O_3 films is estimated using Debye Scherrer's formula:

$$D = \frac{0.94\lambda}{\beta_{2\theta}\cos\theta} \quad (1)$$

where λ is the wavelength of the X-ray and β is the full width at half maximum in radians. The average size of the crystallites calculated for the different films is in the range of 7–32 nm (Table 1). This observation shows that the films are nanocrystalline in nature.

The lattice parameter 'a' is determined by comparing the peak positions (2θ) of the XRD patterns of the films with that of the bulk In_2O_3 using the relation:

$$\frac{1}{d^2} = \frac{h^2 + k^2 + l^2}{a^2} \quad (2)$$

The close matching of the calculated lattice constant 'a' for the films compared with that of the bulk value confirms the presence of indium oxide cubic phase in the films.

A dislocation is an imperfection in a crystal associated with misregistry of the lattice in one part of the crystal with the other part. Unlike vacancies and interstitial atoms, dislocations are not equilibrium imperfections. The growth mechanism involving dislocation is a matter of importance. The dislocation density δ can be evaluated from the particle size (D) by the relation [14]:

$$\delta = \frac{n}{D^2} \quad (3)$$

where n is a factor, which when equals unity gives minimum dislocation density. The dislocation density δ calculated for the films is displayed in Table 1.

The origin of micro-strain (lattice strain ε_S) is related to lattice misfit, which in turn depends on deposition conditions. The lattice strain (ε_S) developed in the In_2O_3 can be calculated from the relation [14]:

$$\varepsilon_S = \left(\frac{\lambda}{D\cos\theta} - \beta\right)\frac{1}{\tan\theta} \quad (4)$$

The biaxial strain $\varepsilon = (a_{film}/a_{bulk}) - 1$ is calculated using XRD data where a_{film} and a_{bulk} are the lattice parameters of the film and the bulk respectively. The negative value of biaxial strain indicates that the crystallites are in a state of compressional strain whereas positive value indicates tensile strain.

In order to understand the effect of the annealing on the stress of the INO thin film, the stress in the films is calculated using the following formula [5]:

$$\sigma = -233 \times 10^9 \left(\frac{a_{film}}{a_{bulk}} - 1\right) \quad (5)$$

The various structural parameters for annealed at different temperatures are calculated using relevant formula and systematically presented in Table 1.

3.2. SEM studies

Granular microstructure of In_2O_3 films as-deposited at different substrate temperatures 473, 623 and 773 K and post-annealed at 773 and 973 K are shown in Figs. 4–6. All the films are nanostructured and the crystallinity of the films increase with the increase in annealing temperature for the films deposited at different substrate temperatures. SEM images (Fig. 4(i) and (ii)) of A films post-annealed at 773 and 973 K show that the films are densely packed with nanocrystalline grains. Fig. 5(i) and (ii) shows the SEM images of post-annealed B films with a well patterned distribution of nanocrystalline grains with porous nature. SEM images (Fig. 6(i)–(iii)) of as-deposited and post-annealed C films also show a well patterned distribution of nanocrystalline grains with porous nature. This open and porous nature of the films B and C renders them suitable for gas sensing applications. The gas sensing property of thin film sensors can be maximized by maximizing the surface area of the material as the gas sensor action of semiconductor metal oxides is a surface phenomenon. This is better accomplished in highly porous films made of nanocrystallites.

3.3. AFM studies

To study the effect of substrate temperature and post-annealing on the surface properties of In_2O_3 films systematically, AFM measurements have been performed on all films with a scan area of 2 μm × 2 μm. Figs. 7(i)–(iii), 8(i)–(iii) and 9(i)–(iii)) show the three-dimensional surface morphology of as-deposited and post-annealed A–C films respectively. The rms surface roughness of the films is calculated and given in Table 2. AFM image of the as-deposited A film (figure not shown) reveals a discontinuous grain growth. As the substrate temperature is increased, the surface diffusion is activated and the surface morphology improves with distinct visible grain boundaries (Figs. 8 and 9(i)). This

Table 1
Effect of substrate temperature and post-deposition annealing on structural parameters of laser ablated In_2O_3 thin films.

In_2O_3 film, T_s (K)	T_{ANN} (K)	Lattice constant, a	Average crystallite size, D (nm)	Dislocation density, δ ($\times 10^{11}$ nm^{-2})	Lattice strain, ε ($\times 10^{-3}$ cm^{-2})	Biaxial strain ($\times 10^{-3}$)	Stress ($\times 10^{9}$ Pa)
473	473	10 114 ± 0.003	18	2.95	2.74	−0.40	0.09
	773	10 138 ± 0.003	6	30.99	6.23	1.97	−0.46
	973	10 141 ± 0.006	8	17.16	4.58	2.27	0.53
623	773	10 127 ± 0.004	17	3.50	3.07	0.71	0.17
	973	10 108 ± 0.004	26	1.49	1.99	−0.99	0.23
773	As-deposited	10 141 ± 0.003	32	0.98	1.14	2.27	−0.53
	773	10 141 ± 0.003	11	8.73	6.09	2.27	−0.53
	973	10 129 ± 0.003	22	2.03	1.57	1.09	−0.25

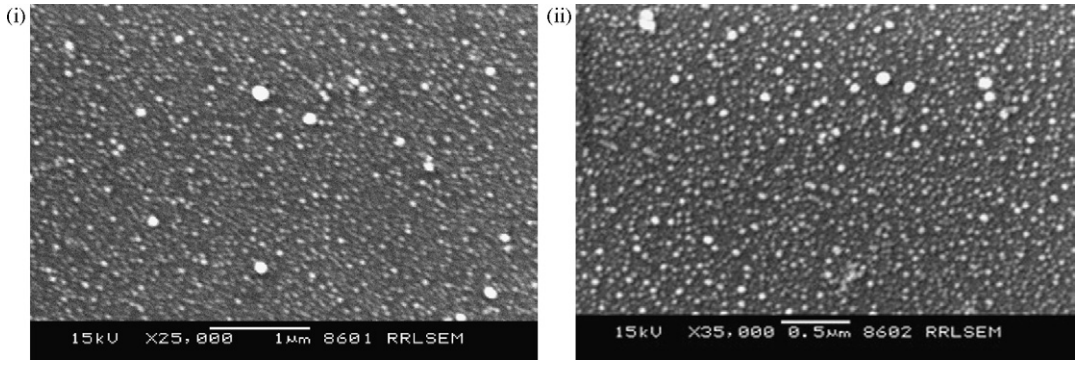

Fig. 4. (i) and (ii) SEM images of as-grown laser ablated indium oxide film deposited at T_s = 473 K and post-annealed films at (i) 773 K and (ii) 973 K

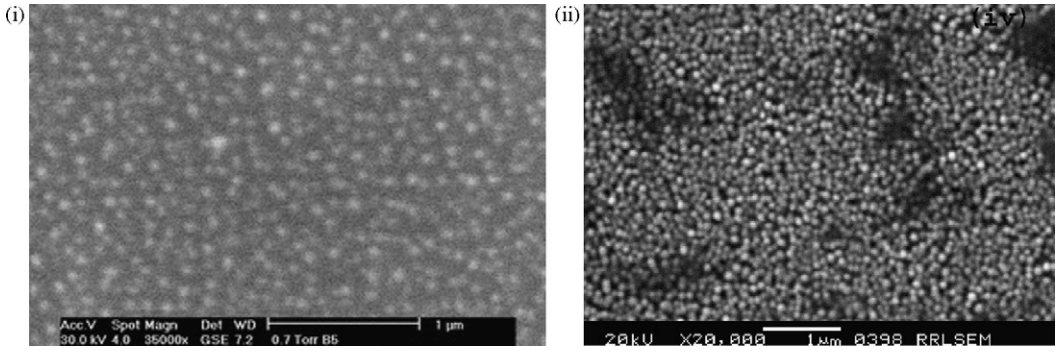

Fig. 5. (i) and (ii) SEM images of as-grown laser ablated indium oxide film deposited at T_s = 623 K and post-annealed films at (i) 773 K and (ii) 973 K.

observation is in agreement with the enhancement in crystalline nature with increase in substrate temperature observed in the XRD measurements.

AFM images (Fig. 7(i)) of the A film post-annealed at 473 K show the onset of island formation. AFM images (Fig. 7(ii)) of the A film post-annealed at 773 K manifest island formation with lack of distinct grain boundary. A self-assembly of grains into rings can be seen in the AFM micrograph (Fig. 7(iii)) of the A film post-annealed at 973 K. The grain boundaries in this film are more distinct compared to other films in this series. The rms surface roughness

Table 2
Variation of band gap, transmittance, rms surface roughness, resistivity and refractive index of as-grown laser ablated indium oxide film deposited at different substrate temperatures and post-annealed at different annealing temperatures.

Sample	Annealing temperature (K)	Band gap, E_g (eV)	Thickness (nm)	Transmittance in 300–900 nm (%)	rms roughness (nm)	Resistivity, ρ (Ω m)	Refractive index of the films at 550 nm region
A	As-deposited	3.71	120	58	–	2.5×10^{-2}	2.226
	473	3.64	130	84	13.47	7.6×10^{-4}	1.932
	773	3.55	142	73	21.31	3.4×10^{-3}	1.943
	973	3.54	150	63	5.86	2.2	2.189
B	As-deposited	3.71	130	64	6.82	3.3×10^{-3}	2.103
	773	3.5	145	56	5.50	4.2×10^{-3}	1.987
	973	3.59	160	41	8.91	1.6×10^{-2}	2.045
C	As-deposited	3.5	180	47	22.51	6.6×10^{-5}	1.892
	773	3.56	195	64	28.17	3×10^{-3}	1.923
	973	3.57	215	56	27.45	2.8×10^{-3}	2.021

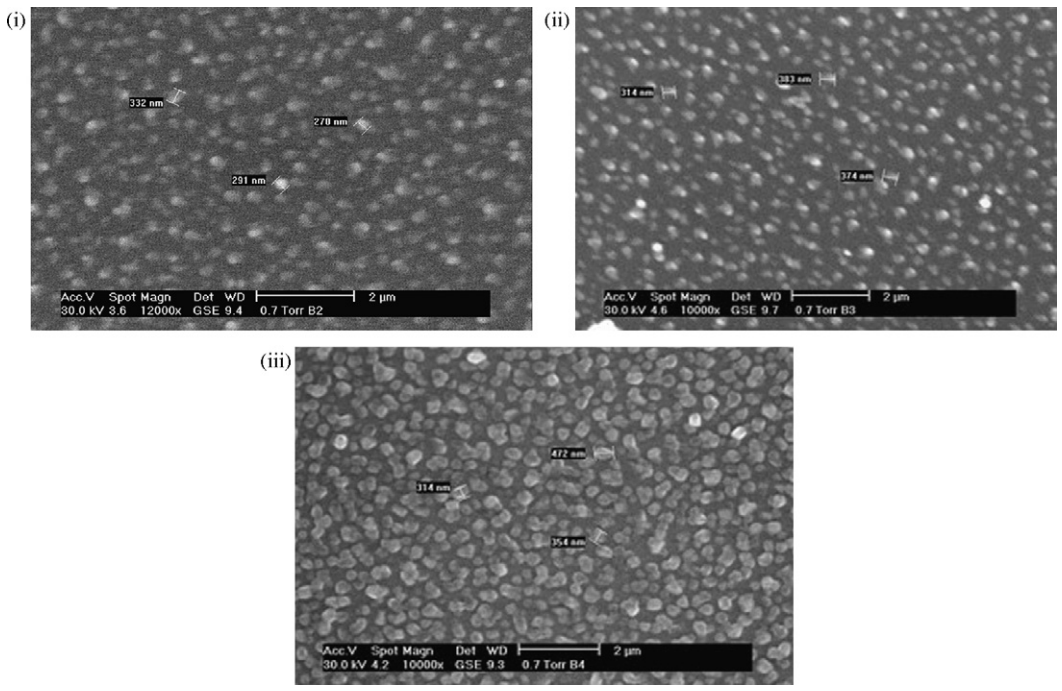

Fig. 6. (i)–(iii) SEM images of as-grown laser ablated indium oxide film deposited at (i) T_s = 773 K and post-annealed films at (ii) 773 K and (iii) 973 K.

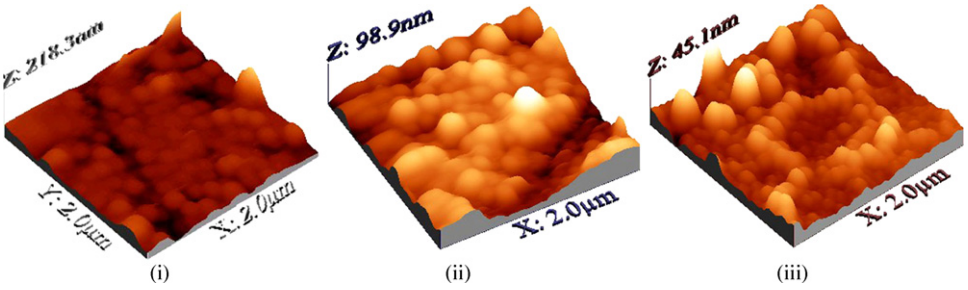

Fig. 7. (i)–(iii) AFM images of as-grown laser ablated indium oxide film deposited at T_s = 473 K and post-annealed films at (i) 473 K, (ii) 773 K and (iii) 973 K.

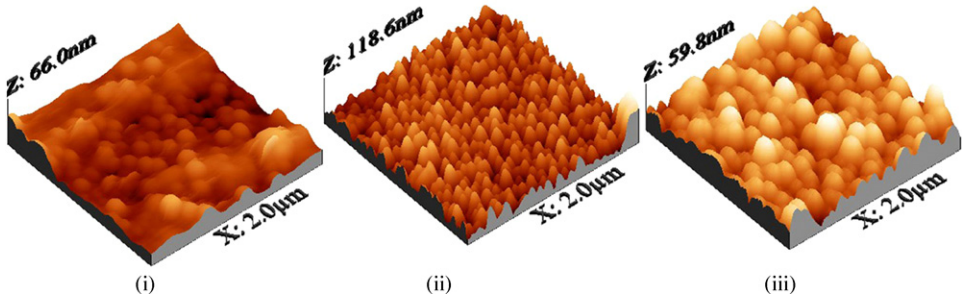

Fig. 8. (i)–(iii) AFM images of as-grown laser ablated indium oxide film deposited at (i) T_s = 623 K and post-annealed at (ii) 773 K and (iii) 973 K.

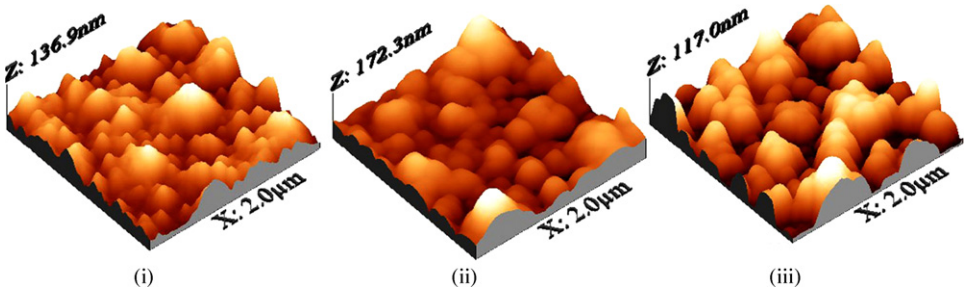

Fig. 9. (i)–(iii) AFM images of as-grown laser ablated indium oxide film deposited at (i) T_s = 773 K and post-annealed at (ii) 773 K and (iii) 973 K.

measured for post-annealed A films is 13.5, 21.3 and 5.9 nm respectively.

Almost continuous and highly agglomerated grain growth can be revealed in the AFM picture for the as-deposited film prepared at substrate temperature 473 K (B film). On post-annealing at 773 K this film presents highly textured surface morphology with columnar grain growth in the AFM picture (Fig. 8(ii)). Well patterned arrangement of grains of larger size with well defined boundaries can be seen in the AFM picture (Fig. 8(iii)) of B film post-annealed at 973 K.

The surface morphology of the as-deposited C film presents continuous growth of grains of different sizes with almost distinct grain boundary (Fig. 9(i)). AFM pictures (Fig. 9(ii) and (iii)) of C film post-annealed at 773 and 973 K reveal the enhancement of grain size due to coalescence of smaller grains. It can also be seen that the films become highly porous at higher annealing temperature. The increased thermal energy and larger mobility acquired by the grains during annealing result in different surface morphologies for films deposited at different substrate temperatures.

3.4. Electrical properties of In_2O_3 films

DC resistivity of the films is measured using Keithley Digital (2400) source meter and is given in Table 2. The as-deposited films show a drastic decrease in electrical resistivity with increase in substrate temperature. The observed values of dc electrical resistivity of the as-deposited A–C films are 2.5×10^{-2}, 3.3×10^{-3} and $0.66 \times 10^{-6}\ \Omega$ m respectively. Lack of stoichiometry in the indium oxide films due to the presence of oxygen-array vacancies and the oxygen vacancies can act as doubly ionized donors which can contribute two electrons for electric conduction. Since the films are deposited in a non-reactive atmosphere, an enhancement in the number of oxygen vacancies and hence higher carrier density can be expected in the film due to oxygen desorption at high substrate temperatures. This enhancement in the carrier density due to oxygen desorption with increase in substrate temperature can be one of the reasons for the observed drastic decrease in electrical resistivity with increase in substrate temperature in the as-deposited indium oxide films. The XRD, SEM and AFM analysis point to an improved order and crystalline nature for the as-deposited films deposited at higher substrate temperatures. When the film becomes more ordered and crystalline, the scattering and trapping centers of electric carriers become less and hence electric conductivity increases [20]. Indium oxide films of high resistivity are deposited by PLD at low oxygen pressures below 0.0013 mbar [21]. Minimum resistivity reported for the In_2O_3 films (deposited by different techniques) is of the order of $2.2 \times 10^{-6}\ \Omega$ m and has been deposited at room temperature in the pressure range of 0.013–0.019 mbar [21]. In the present case the as-deposited film prepared at substrate temperature 773 K shows a still lower dc resistivity value ($0.66 \times 10^{-6}\ \Omega$ m)

For all the films, except the A film annealed at 473 K, the value of dc electrical resistivity increases with increase in annealing temperature. This can be due to the depletion of oxygen vacancies when the films are annealed in oxygen ambience. As explained in AFM analysis the A film presents only a discontinuous grain growth. A comparatively continuous grain growth exhibited by A film annealed at 473 K can be the reason for its observed lower value of resistivity.

3.5. Optical properties of In_2O_3 films

Fig. 10(i)–(iii) represents the optical transmittance spectra of as-deposited and annealed A–C films respectively. The as-deposited A film shows only a relatively low value of average optical transmittance (~58%) in the wavelength range of 300–900 nm. Enhanced scattering loss due to discontinuous grain growth can be the reason for the low transmittance of this film. All the annealed A films show higher value of average optical transmittance compared to that of the as-deposited film. This can be due to the improved crystallinity and order in the annealed films. The A film annealed at T_{ANN} = 473 K exhibits the highest value of transmittance (~84%). Interestingly this film shows a comparatively lower value of electrical resistivity of $0.76 \times 10^{-5}\ \Omega$ m. This observation can be of immense importance in solar cell application point of view. The film annealed at 773 K shows a slight reduction in optical transmittance to 73%. This can be due to enhanced rms surface roughness, increased thickness and decrease in the value of crystallite size. As the size of the crystallite decreases the grain boundary scattering increases and hence optical transmittance can be reduced. The film annealed at 973 K exhibits more absorption in the 300–600 nm region and the value of transmittance decreases to an average value 63%. We do not have proper explanation for this absorption shown by this film.

The transmittance of as-deposited B film prepared at substrate temperature 623 K shows an average transmittance of 64%. The better transmittance shown by this film compared to that of the as-deposited A film can be due to the enhanced crystallinity. Post-annealing decreases the transmittance of B films although the crystallinity increases on annealing. The SEM and AFM images show a porous nature for the annealed films. The increased thickness, randomly oriented grain growth and porous nature for the annealed films can be the reason for the decrease in transmittance.

The transmittance of as-deposited C film prepared at substrate temperature773 K shows the lowest value for average transmittance (47%). On annealing at T_{ANN} = 773 K the average transmittance increases to ~65% in the wavelength range of 300–900 nm, which can be due to the depletion of oxygen vacancies. However at T_{ANN} = 973 K the transmittance decreases to 56%. This decrease in transmittance compared to the film annealed at 773 K can be due to the enhanced grain boundary scattering.

The transmittance data obtained for the films are used to calculate the absorption coefficients at different wavelengths using the following relation:

$$T = \exp(-\alpha t) \tag{6}$$

where t is the film thickness and T is the transmittance of the film. The optical band gap E_g can be estimated from the following relation which is known as the Tauc plot [22]:

$$\alpha h\nu = A(h\nu - E_g)^n \tag{7}$$

where A is a constant, ν is the transition frequency and the exponent n characterizes the nature of band transition. n = 1/2 and 3/2 correspond to direct allowed and direct forbidden transitions and n = 2 and 3 correspond to indirect allowed and indirect forbidden transitions respectively [23–25]. The band gap can be obtained from extrapolation of the straight-line portion of the $(\alpha h\nu)^{1/n}$ vs. $h\nu$ plot to $h\nu$ = 0. It is observed that for the as-deposited and annealed films of samples A–C the best straight line is obtained for n equal to 1/2 which is expected for direct allowed transition. Calculated band gap values are given in Table 2.

The observed band gap value for the as-deposited film A film is 3.71 eV and on annealing at temperatures 473, 773 and 973 K band gap values decrease to 3.64, 3.55 and 3.54 eV respectively. Due to amorphous nature, the crystallite size of the as-deposited film is not known. The average size of the crystallites calculated from the Debye Scherrer's formula, for the A films annealed at temperatures 473, 773 and 973 K is 18, 6 and 8 nm respectively. Due to quantum confinement effect, the values of the band gap energy increase with decrease in crystallite size [26,27]. But in the case of annealed A films the variation of values of band gap energy is not in accordance with particle size variation. Srikant and Clark [28], Dutta et al. [29] and Navas et al. [30] have reported similar observation of decrease in band gap energy with decrease in particle size. In nanocrystalline

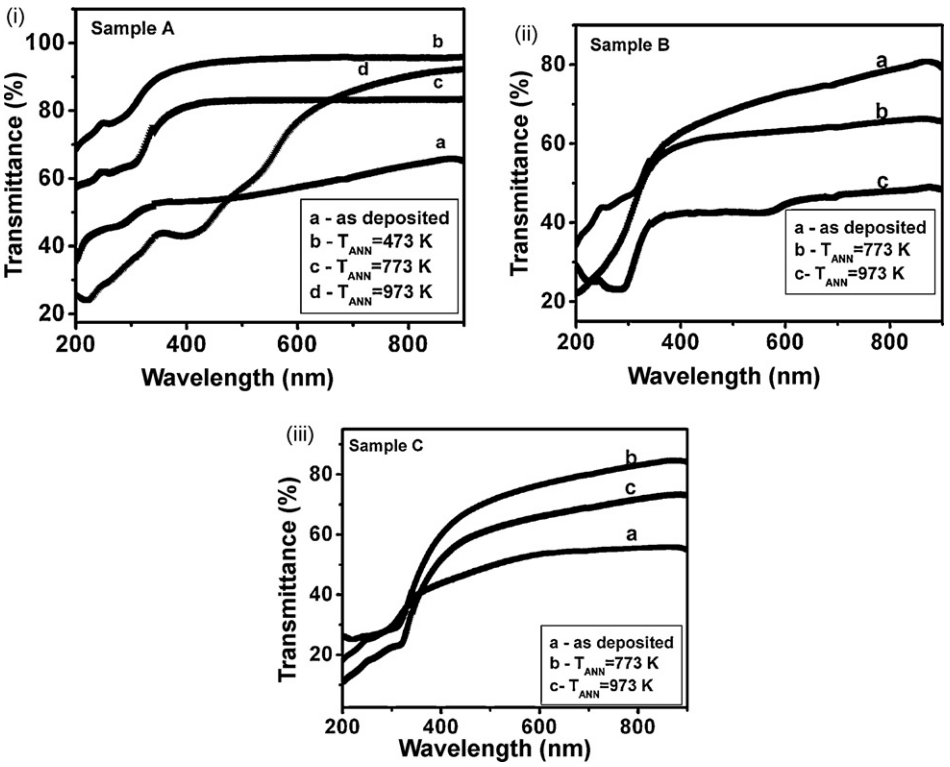

Fig. 10. (i)–(iii) Optical transmission spectra of as-grown laser ablated indium oxide film deposited at (i) T_s = 473 K, (ii) T_s = 773 K and (iii) T_s = 973 K.

materials the surface to volume ratio is higher and band bending can be expected at the grain boundaries. In crystallites with smaller size, the band bending effect will be more compared to bigger crystallites. In bigger grains the band edge becomes sharp and band gap can be wider than that of smaller grains. Hence the observed decrease in band gap energy with decrease in particle size can be attributed to band bending effect at the particle boundaries [28–30] as the grain size decreases at higher annealing temperature of 773 and 973 K.

The observed band gap for the as-deposited B film is 3.71 eV and on annealing at 773 and 973 K band gap values decrease to 3.5 and 3.59 eV respectively. As-deposited and annealed C films are having band gap of the order 3.5–3.57 eV. The band gap variations are less on C films on annealing compared to that of both A and B films.

According to the analysis given by Pankove [31], the transmission in the absence of interference fringes of a thin film deposited on a perfectly smooth substrate is given by

$$T = \frac{(1-R)^2 \exp(-at)}{1-R^2 \exp(-2at)} \tag{8}$$

where t is the film thickness and α is the absorption coefficient ($\alpha = 4\pi k/\lambda$).

For normal light incidence, the reflectivity, R may be expressed in terms of the real refractive index, n, and the extinction coefficient, k, by

$$R = \frac{(n-1)^2 + k^2}{(n+1)^2 + k^2} \tag{9}$$

Solving Eq. (7) for n gives

$$n = \frac{1+R+\sqrt{4R-(1-R)^2k^2}}{1-R} \tag{10}$$

The refractive index of the films is evaluated from the spectra and the values of refractive index corresponding to 550 nm are given in Table 2. These values are in the range of 1.89–2.23. A value of 1.84 is reported for the refractive index for sol–gel In_2O_3 films [32] and values 1.90–2.24 are also reported for rf sputtered In_2O_3 films [33].

3.6. Photoluminescence of In_2O_3 films

Room temperature photoluminescence spectra recorded for In_2O_3 films A–C are respectively given in Figs. 11–13. The PL spectra of films A–C are recorded using an excitation wavelength at 255 nm. The as-deposited film of sample A shows very broad PL spectral features compared to the annealed films. The spectrum of the as-deposited film shows peaks centered around 293, 397, 420 and 468 nm. The annealed samples show UV emission peaks at 280 and 390 nm regions. In general emission spectra can be divided into two broad categories: the near band edge (NBE) emission and deep-level (DL) emission [16]. High crystal quality and the quantum confinement effect related to the nanostructures are two factors favoring the increase of intensity of UV emission at

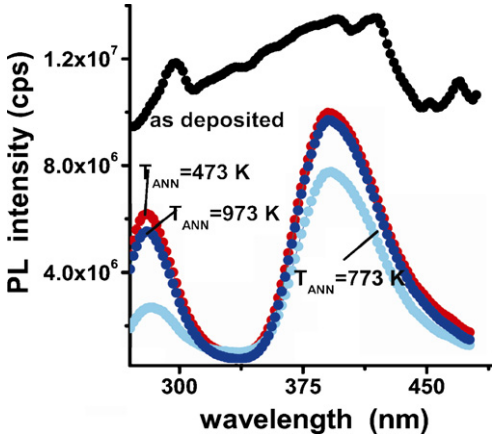

Fig. 11. Photoluminescence spectra of laser ablated In_2O_2 film A.

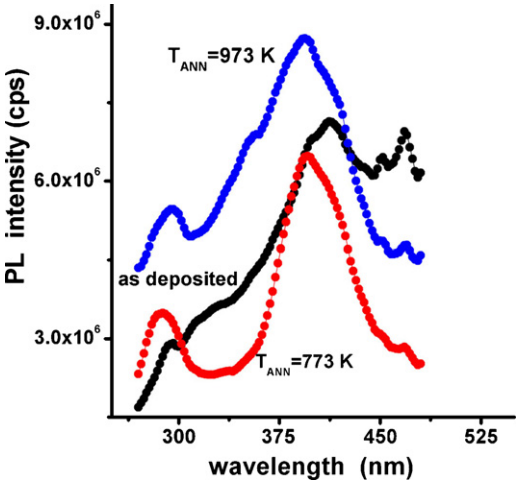

Fig. 12. Photoluminescence spectra of laser ablated In_2O_3 film B.

room temperature. High crystal quality of INO nanoparticles may be attributed to the annealing process, which can decrease impurities and structure defects such as oxygen vacancies. This leads to a high NBE-emission-to-DL-emission ratio, which results in a detectable UV emission at room temperature [34,35]. The peak at 397 nm is due to near band edge emission owing to excitonic transition [17]. The indium oxide films particularly the as-deposited film contain large number of defects due to oxygen vacancies. Oxygen vacancies can induce the formation of energy levels in the energy band. The PL peaks at 420, 452 and 470 nm shown by the as-deposited film can be contributed by imperfections and defects due to oxygen vacancies [15,36,37]. The absence of these PL peaks in the spectra of the annealed samples (Fig. 11) supports this conclusion. Annealing process reduces the impurity sites and structural defects such as oxygen vacancies.

Fig. 12 shows the PL spectra of the as-deposited and annealed films of sample B. PL spectra exhibited by sample B less intense compared to that of sample A. The as-deposited film shows a broad spectral feature with intensity maximum around 397 and 412 nm. The intensity of the peak at 412 nm is larger compared to that at 397 nm. This indicates that the defect related emission is more compared to near band edge emission in the as-deposited film B. The PL spectrum also shows two peaks at 450 and 468 nm due to oxygen vacancies. It can be seen that the intensity of the PL peak around 396 nm increases whereas the intensity of peaks around 420, 452 and 470 decreases with increase in annealing temperature. This observation also is in support of the earlier conclusion drawn for sample A. There is a slight blue shift for the UV emission peak with increase in annealing temperature for sample B. This observation is in agreement with the increase in optical band gap on annealing. The PL spectra of as-deposited and annealed films of sample C are given in Fig. 13. The as-deposited film shows a narrow spectral feature with intensity maximum around 396 nm corresponding to near band edge emission. There are also peaks at 294 and 470 nm indicating defects and oxygen vacancies. It can be seen that the intensity of the PL peak around near band edge emission increases whereas the intensity of defect related peaks decreases with increase in annealing temperature. There is a slight blue shift for the UV emission peak at T_{ANN} = 773 K which is consistent with our XRD and AFM results. At T_{ANN} = 973 K, The peak at 393 nm is suppressed and the peak at 553 nm enhances. The photoluminescence emission in the UV region at room temperature for the films suggests possible applications of these films in nanoscale optoelectronic devices in the future. Efficient photoluminescence emission is observed in all the films and this can be attributed to higher values of rms surface roughness exhibited by these films. In films with higher rms surface roughness, the loss of light energy due to internal reflection within the film will be less and this can result in very intense PL emission. Similar effects are reported in Eu^{3+} doped Gd_2O_3 thin film phosphor by Seo et al. [38], Li doped Gd_2O_3:Eu^{3+} thin film phosphor by Soung-soo et al. [39] and Gd substituted Y_2O_3:Eu^{3+} thin film phosphor by Dae et al. [40].

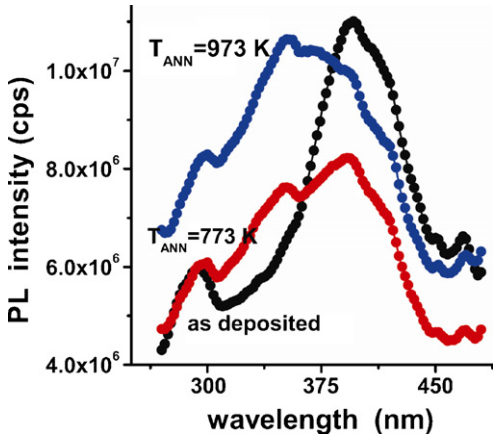

Fig. 13. Photoluminescence spectra of laser ablated In_2O_3 film C.

3.7. Conclusions

Polycrystalline thin In_2O_3 films of nanocrystalline nature are deposited on quartz plates at different substrate temperatures and subjected to post-annealing at 473, 773 and 973 K. SEM images and AFM pictures show porous nanocrystalline nature for the films of samples B and C which make them suitable for gas sensing. The increased thermal energy and larger mobility acquired by the grains during annealing result in different surface morphologies for films deposited at different substrate temperatures. The as-deposited films show a drastic decrease in electrical resistivity with increase in substrate temperature. A red shift of the absorption edge is observed for the annealed films which may be due to the effect of band bending at the grain surface. Efficient photoluminescence emission observed in all the films can be attributed to higher values of rms surface roughness exhibited by these films. In_2O_3 films exhibit a PL emission property in the UV region at room temperature which suggests possible applications in nanoscale optoelectronic devices in the future.

References

[1] D. Liu, W.W. Lei, B. Zou, S.D. Yu, J. Hao, K. Wang, B.B. Liu, Q.L. Cui, G.T. Zou, J. Appl. Phys. 104 (2008) 083506.
[2] R.L. Weiher, R.P. Ley, J. Appl. Phys. 37 (1966) 299.
[3] C. Li, D. Zhang, S. Han, X. Liu, T. Tang, C. Zhou, Adv. Mater. 15 (2003) 143.
[4] Z.L. Wang, J. Song, Science 312 (2006) 242.
[5] Zh. Pan, Z. Dai, Z.L. Wang, Science 291 (2001) 1947.
[6] W.S. Seo, H.H. Jo, K. Lee, J.T. Park, Adv. Mater. 15 (2003) 795.
[7] C. Li, D. Zhang, X. Liu, S. Han, T. Tang, J. Han, C. Zhou, Appl. Phys. Lett. 82 (2003) 1613.
[8] K. Soulantica, L. Erades, M. Sauvan, F. Senocq, A. Maisonnat, B. Chaudret, Adv. Funct. Mater. 13 (2003) 553.
[9] C. Li, B. Lei, D. Zhang, X. Liu, S. Han, T. Tang, M. Rouhanizadeh, T. Hsiai, C. Zhou, Appl. Phys. Lett. 83 (2003) 4014.
[10] X. Li, M.W. Wanlass, T.A. Gessert, K.A. Emery, T.J. Coutts, Appl. Phys. Lett. 54 (1989) 2674.
[11] K. Sreenivas, T. Sudersena Rao, A. Mansingh, J. Appl. Phys. 57 (1985) 384.
[12] Y. Shigesato, S. Thalaki, T. Haranob, J. Appl. Phys. 71 (1992) 3356.
[13] D. Beena, K.J. Lethy, R. Vinodkumar, V.P. Mahadevan Pillai, Solar Energy Mater. Solar Cells 91 (2007) 1438.
[14] A. Salehi, Thin Solid Films 324 (1998) 214.
[15] H.J. Zhou, W.P. Cai, L.D. Zhang, Appl. Phys. Lett. 75 (1999) 495.
[16] M.J. Zhang, L.D. Zhang, G.H. Li, X.Y. Zhang, X.F. Wang, Appl. Phys. Lett. 79 (2001) 839.

[17] H. Cao, X. Qiu, Y. Liang, Q. Zhu, Appl. Phys. Lett. 83 (2003) 761.
[18] D.B. Cullity, Elements of X-ray Diffraction, Addison-Wesley Inc., Massachusetts, 1956.
[19] JCPDS Card No. 06-0416.
[20] R.B.H. Tahar, T. Ban, Y. Ohiya, Y. Takahashi, J. Appl. Phys. 83 (5) (1998) 2631.
[21] F.O. Adurodija, H. Tzumi, T. Ishihara, H. Yoshioka, M. Matsui, M. Motoyamma, Appl. Phys. Lett. 74 (1999) 3059.
[22] J. Tauc, Amorphous and Liquid Semiconductors, Plenum, London, 1974, p. 159.
[23] A. Goswami, Thin Film Fundamentals, New Age International (P) Limited, New Delhi, 1996.
[24] J.R. Rani, V.P. Mahadevan Pillai, R.S. Ajimsha, M.K. Jayaraj, R.S. Jayasree, J. Appl. Phys. 100 (2006) 014302.
[25] K.J. Lethy, D. Beena, R. Vinodkumar, V.P. Mahadevan Pillai, Appl. Surf. Sci. 254 (2008) 2369.
[26] Al.L. Efros, A.L. Efros, Sov. Phys. Semicond. 16 (1982) 772.
[27] Y.G. Wang, S.P. Lau, H.W. Lee, S.F. Yu, B.K. Tay, X.H. Zhang, H.H. Hng, J. Appl. Phys. 94 (2003) 354.
[28] V. Srikant, D.R. Clark, J. Appl. Phys. 81 (1997) 6357.
[29] S. Dutta, S. Chattopadhyay, M. Sutradhar, A. Sarkar, M. Chakrabarti, D. San yal, D. Jana, J. Phys.: Condens. Matter 19 (2007) 236218.
[30] I. Navas, R. Vinodkumar, K.J. Lethy, M. Satyanarayana, V. Ganesan, V.P. Mahadevan Pillai, J. Nanosci. Nanotechnol. 9 (2009) 5254.
[31] J.I. Pankove, Optical Process in Semiconductors, Dover, New York, 1971.
[32] R.B.H. Tahar, T. Ban, Y. Ohiya, Y. Takahashi, J. Appl. Phys. 82 (2) (1997) 865.
[33] F.O. Adurodija, L. Semple, B. Bruning, Thin Solid Films 492 (2005) 153.
[34] Y.C. Kong, D.P. Yu, B. Zhang, W. Fang, S.Q. Feng, Appl. Phys. Lett. 78 (2001) 407.
[35] D.M. Bagnail, Y.F. Chen, Z. Zhu, T. Yao, S. Koyama, N.Y. Shen, T. Goto, Appl. Phys. Lett. 73 (1998) 1038.
[36] M.S. Lee, W.C. Chjoi, E.K. Kim, S.D.K. Min, Thin Solid Films 279 (1996) 1.
[37] C. Liang, G. Meng, Y. Lei, F. Philipp, L. Zhang, Adv. Mater. 13 (2001) 1330.
[38] S.Y. Seo, S. Lee, H.D. Park, N. Sheh, K.S. John, J. Appl. Phys. 92 (2002) 5248.
[39] Y.I. Soung-soo, J.S. Dae, K.S. Shim, J.H. Jeong, S.-C. Park, P.H. Holloway, Appl. Phys. Lett. 84 (2004) 353.
[40] J.S Dae, J.H Jeong, Y.I Soung-soo, S.-C. Park, Appl. Phys. Lett. 82 (2003) 3629.